PAPER

Check for updates

Interface layer chemistry dependent oxygen defect formation in BaZrO₃(110)/SrTiO₃(100) heterostructures

Jason Rakowsky and Pratik P. Dholabhai [ID] *

Mismatched complex oxide thin films and heterostructures based on perovskites have key applications in technologies such as solid oxide fuel cells, batteries, and solar cells because of emerging properties at the interface. Although lattice mismatch and resulting misfit dislocations are one of the fundamental reasons for the emergence of new properties at the interface, their precise role is not well understood. In light of this, we have used first principles calculations to study BaZrO₃(110)/SrTiO₃(100) heterostructures for thin film electrolyte applications and predict the interfacial stability as a function of termination layer chemistry. Atomic scale structure and electronic structure of oxygen vacancies at doped interfaces was further studied to comprehend their stability and location preference at the interface. Strong dependence of oxygen vacancy formation on termination layer chemistry is observed. Among the four possible interfaces, oxygen vacancies exhibit a thermodynamic preference to form at the TiO₂–ZrO₂ interface. Results herein shed light on the fundamental aspects of mismatched perovskite oxide interfaces and their influence on thermodynamic stability of oxygen vacancy defects, which influences ionic transport and is imperative to design next-generation thin film oxide electrolytes.

1. Introduction

Thin films and heterostructures based on complex oxides[1–3] exhibit superior and emergent properties[4–6] than their individual constituents. They have gained prominence due to applications in a wide range of nanotechnologies that include solid oxide fuel cells (SOFCs),[7,8] radiation tolerant nuclear materials,[9] information storage,[10] batteries,[11] and catalysts.[12] SOFCs,[13–15] an electrochemical conversion device that produce electricity directly from oxidizing a fuel are highly efficient and a reliable source of clean generation of electrical power. Due to the ever-growing miniaturization of SOFCs, the role of surfaces and interfaces has received increased scrutiny. In SOFCs, solid ceramic oxide electrolyte is one of the most important components since it facilitates the passage of oxide ions that conduct electricity. Since high ionic conductivity is imperative for the development of next-generation SOFCs, significant research efforts have been dedicated toward the discovery and design of thin film oxide electrolytes that allow faster ionic diffusion in the intermediate-temperature (IT) range of 773–973 K.[7,15,16] Thin film oxide electrolytes exhibit superior performance at lower temperatures, wherein interfaces play a crucial role. As a result, widespread use of IT-SOFC electrolytes

requires the basic understanding of the role of interfaces in shaping enhanced performance.[15–17]

In semi-coherent oxide heterostructures, misfit dislocations originate at the heterointerface to mitigate the misfit strain between the two mismatched oxides. Since misfit dislocations are inevitable and responsible for controlling vital material properties,[8,18–20] recent studies have focused on investigating their basic role in influencing material properties. Nonetheless, their impact on ionic transport is not well understood since studies focused on elucidating the atomic and electronic structure of misfit dislocations are limited due to challenges in characterizing individual columns of atoms at the heterointerface. Owing to their ubiquity in semi-coherent oxide heterostructures and their potential impact on material properties, recent computational and experimental studies have investigated the structure–property relationships at misfit dislocations.

Depending on the desired application, perovskites are often doped to enhance magnetic,[21] ionic,[22] electronic,[23] optical, and catalytic[24] properties. SrTiO₃ (STO)[25] and BaZrO₃ (BZO) are one of the most widely studied perovskites, wherein doping is routinely used to tune their functionality. For instance, owing to their versatility, perovskite oxide heterostructures have found applications in SOFCs, wherein they have been studied as model systems for understanding ionic transport across oxide interfaces. Due to the compositional flexibility of perovskite lattice (ABO₃), dopants can replace either A-site, B-site, or O-site ions.

School of Physics and Astronomy, Rochester Institute of Technology, Rochester, NY 14623, USA. E-mail: pratik.dholabhai@rit.edu

Present work will be primarily focused on fundamental factors influencing the oxygen vacancy formation in STO/BZO heterostructures for ionic transport applications. As a result, we limit the discussion to acceptor doping (p-type),[26] wherein the B-site cations, either Ti^{4+} in STO or Zr^{4+} in BZO, could be substituted with trivalent dopants. This doping strategy has been studied in STO[27] and BZO[28] since it leads to the formation of oxygen vacancies (ionic carriers) to maintain the defect equilibria. In this doping scheme, a multitude of aliovalent dopants have been added to boost the properties of STO[29–36] and BZO.[28,37,38]

The added impurities bring their own challenges as they induce physical and chemical changes in the materials through segregation at surfaces and interfaces, which primarily depends on size mismatch and charge interactions,[39] formation of space-charge layers at interfaces,[40] and growth conditions and post-deposition annealing procedures.[41] Since segregated additives could lead to deleterious effects on material stability and performance, understanding the role of aliovalent dopants and concomitant vacancies in complex oxides is crucial. In fast ion conductors, the influence of dopants is critical as they are primarily introduced to increase the oxygen vacancy fraction, but their presence on the cation sublattice influences oxygen vacancy formation and dynamics on the anion sublattice. Oxygen vacancy formation[42] and migration[43–49] in doped bulk perovskite oxides have been reported, wherein density functional theory (DFT) calculations and simulations based on interatomic potentials have been the method of choice. However, oxygen vacancy formation at perovskite oxide heterointerfaces is not well understood.

At mismatched interfaces, it is imperative to understand the basic role of trivalent dopants and resulting oxygen vacancies that are accountable for ionic conduction. At interfaces and misfit dislocations in BZO/STO heterostructures, how dopants influence oxygen vacancy formation is not well understood since the majority of reported work is focused on either bulk STO or bulk BZO. An exception to this is our recent study, which utilized atomistic simulations based on interatomic potentials to predict oxygen vacancy formation and migration in STO(100)/BZO(100) heterostructures. To the best of our knowledge, except our recent work, which was performed using atomistic simulations, there are no studies in the literature that report oxygen vacancy formation near misfit dislocations in BZO/STO heterostructures. Since STO[50] and BZO[28] are technologically relevant with potential applications as SOFC electrolytes,[8,51–53] oxide heterostructures synthesized using either of them have garnered recent interest.[54–56] A lack of understanding pertaining to basic ionic transport mechanisms in thin film SOFC electrolytes exists in the field mainly due to challenges in experimentally visualizing dopant atoms, characterizing oxygen vacancies, and resolving the structure and chemistry of misfit dislocations. The problem is further compounded as even from a theoretical perspective, calculations that utilize DFT are limited to coherent interfaces to keep the supercell size tractable.[57] As a result, DFT calculations to study oxygen vacancy migration at misfit dislocations necessitate very large supercells, which is computationally challenging. For instance, in STO(100)/BZO(100) heterostructures, we have shown using atomistic simulations that oxygen vacancy migration energy barriers[58]

and thermodynamic stability of dopant-defect complexes[59] depend on both interface termination and misfit dislocation structure. Nonetheless, since these studies utilized atomistic simulations, we could afford large supercells comprising ∼21 900 atoms, which is beyond the realm of DFT simulations. To address this challenge, we used an approach wherein we rotated the BZO thin film by 45°, which increased the misfit strain with the STO substrate, allowing us to study misfit dislocations in smaller supercells for BZO(110)/STO(100) heterostructures. To effectively use DFT simulations, we have successfully implemented a similar strategy to predict structure–property relationships in oxide heterostructures.[60]

In perovskite oxides, defects could typically introduce ligand holes, which could further lead to altered magnetic properties as observed in STO.[61] Moreover, oxygen vacancy formation and migration in perovskites could be influenced by change in oxidation states of added impurities having mixed valence, which could offer routes for tailoring mixed ionic electronic conductors in SOFCs.[62] However, in the present work, we strictly focus on studying the role of defects (oxygen vacancies) that are formed to maintain the defect equilibria after incorporation of trivalent dopants that do not exhibit mixed valence. Knowledge of oxygen vacancy formation and stability of various terminations in thin film SOFC electrolytes, which in our case is perovskite oxide heterostructures, would be beneficial to understand ionic transport. Vitally, this knowledge will assist in interpreting experimental observations, which have often reported mixed results on the performance of thin film oxide electrolytes. To achieve this goal, we utilized first principles DFT calculations to predict oxygen vacancy formation and interface charge transfer in the model system of BZO(110)/STO(100) heterostructure.[63] To determine the role of interface layer chemistry, we studied the thermodynamic stability of BaO–SrO, SrO–ZrO_2, BaO–TiO_2, and ZrO_2–TiO_2 interfaces as well as predict oxygen vacancy formation in the neighborhood of their dissimilar misfit dislocation structures.[63] The ultimate goal of this work is to offer basic insights into the atomic scale structure and electronic structure of interfaces in BZO(110)/STO/(100) heterostructures and their impact on defect stability, which is expected to influence ionic transport.

It is imperative to note that the primary mechanism for ionic conduction in SOFC electrolytes is oxygen vacancy diffusion mechanism, which has two main contributions – vacancy formation energy and vacancy migration energy. While we have explicitly computed oxygen vacancy formation at dissimilar interface locations, studying oxygen vacancy migration is beyond the scope of this study. One of the main reasons is that these calculations are computationally very intensive, especially at oxide interfaces. For instance, in comparison to bulk, oxide heterointerfaces have hundreds of thousands of disparate migration energy pathways, which are nontrivial to compute from first principles. To this end, as reported in our previous work, we have implemented a strategy wherein migration energy barriers for hundreds of thousands of disparate migration pathways are computed using atomistic simulations,[58] which are used as input to the kinetic lattice Monte Carlo (KLMC) model to trace oxygen vacancy diffusion.[64]

2. Methodology

2.1 Computational details

Spin-polarized calculations were performed using the generalized gradient approximation (GGA) to DFT[65,66] with the Perdew–Burke–Ernzerhof (PBE)[67] exchange correlation functional. Within the GGA formalism, the Kohn–Sham equations were solved using the plane wave basis and used with projected augmented wave (PAW)[68] method as implemented in the Vienna *ab initio* Simulation Package (VASP).[69,70] Numerical errors could arise for DFT calculations of transition metal oxides due to partially filled valence d shells. To address this issue and to account for the strong on-site Coulomb repulsion amid the localized Ti 3d electrons, the rotationally invariant form of GGA+U,[71] a combination of the standard GGA and a Hubbard Hamiltonian for the Coulomb repulsion and exchange interaction, was utilized. For all calculations, U_{eff} value of 4.0 was applied, which has been used for similar systems involving Ti 3d electrons. A plane-wave cutoff energy of 400 eV was utilized, which converged the energies to approximately 0.01 meV. Ground state geometries of different systems were obtained by minimizing the Hellman–Feynman forces until the total forces on each atom were less than 0.02 eV Å^{-1}. The irreducible Brillouin-zone integrations were performed using Monkhorst–Pack grid[72] of $2 \times 2 \times 1$ with Gaussian smearing of 0.1 eV. Large-scale DFT+U calculations were performed using resources from the Advanced Cyberinfrastructure Coordination Ecosystem: Services & Support (ACCESS) program.

2.2 Model heterostructure

Experimental lattice parameters for the two perovskites used in this work are a_{STO} = 0.3905 nm and a_{BZO} = 0.4197 nm. As a result, for cube-on-cube orientation relationship, the lattice mismatch of ~7.0% resulting from this orientation relationship is accommodated *via* the formation of misfit dislocations at the heterointerface. To model this misfit strain *via* inclusion of misfit dislocations, very large atomic models with thousands of atoms are necessitated, which is not realistic for DFT calculations. To address this challenge as well as ensure the presence of misfit dislocations, we rotated the BZO thin film by 45°, which increased the lattice epitaxial strain with the STO substrate to ~23%. Nonetheless, this high epitaxial strain should not be misconstrued as the final strain in the system. This approach allowed us to study misfit dislocations in smaller supercells for BZO(110)/STO(100) heterostructures. For instance, starting with the DFT optimized lattice constants of a_{STO} = 0.3945 nm and a_{BZO} = 0.4256 nm, BZO was rotated by 45° along the z-axis, creating a relative lattice constant of 0.3009 nm. This results in an interface orientation relationship of $[1\bar{1}0]_{BZO}||$-$[010]_{STO}||$interface and $[110]_{BZO}||[100]_{STO}||$interface (Fig. 1). By matching 4 unit cells of BZO with 3 units cells of STO, a 170-atom heterostructure was constructed (Fig. 1) with dimensions 1.191 × 1.191 × 2.763 nm^3. After the rotation of the thin film, since 4 unit cells of BZO (110) are overlaid on 3 unit cells of STO (100), the resulting residual strain in the heterostructures is ~1%, which is further mitigated by lattice relaxation at the interface that minimizes the total potential energy *via* reduction in elastic strain energy. This approach allowed us to predict misfit dislocation structure and study fully relaxed heterostructures that are fairly accurate representation of experimentally synthesized materials. We have successfully used a similar recipe[60,73] in the past to predict and study misfit dislocation structure and correlate them with experimentally observed properties of oxide heterostructures.[74–76]

To limit the system size, only four layers are included for the film and the substrate. The rationale for the choice of this system size is based on extreme demand on computational resources for larger system sizes, coupled with the fact that there are four heterostructure models to examine. It is imperative to note that this approach and similar system sizes have been used by researchers to study oxide thin films and superlattices.[77–79] Vitally, we have shown that fundamental trends in interface stability and defect energetics obtained from smaller supercells used in DFT calculations[60] agree very well with molecular dynamics simulations performed for larger supercells,[73] as well as offer qualitative agreement with experimental observations.[75,76] As a result, we expect the current approach and system sizes to have sufficient physical fidelity to provide physically meaningful trends. A vacuum layer of 1.5 nm was introduced in the z-direction (supercell thickness) to avoid periodic interaction
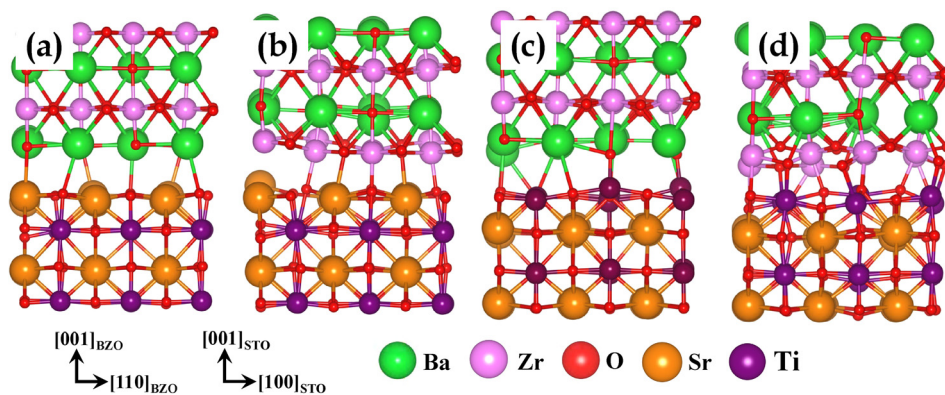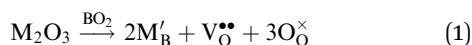

Fig. 1 Side view of the atomic scale structure of energetically minimized BZO/STO heterostructures for four different terminations of the interface layer for (a) BaO–SrO (b) ZrO$_2$–SrO (c) BaO–TiO$_2$ and (d) ZrO$_2$–TiO$_2$ interfaces. Interface orientation relationship is shown below the panels. Green, pink, red, brown, and violet spheres correspond to Ba, Zr, O, Sr, and Ti ions, respectively.

between misfit dislocations and defects. This strategy ensures only one interface is present in the model. Periodic boundary conditions were implemented in all three supercell directions. Using this approach, four stochiometric BZO(110)/STO(100) heterostructures were constructed with different terminations and interface layer chemistries. *i.e.*, BaO–SrO, SrO–ZrO$_2$, BaO–TiO$_2$, and ZrO$_2$–TiO$_2$ interfaces.

2.3 Defect energy formalism

Various trivalent dopants can be added to improve the properties of perovskites, as their net effective charge affects the electroneutrality condition, and thus the defect equilibria.[29–31,37] In perovskites, trivalent dopants can replace either of the cations on the A and B sublattices. Since the current work is focused on ionic transport in perovskite heterostructures, we have exclusively studied acceptor doping (p-type),[26] wherein Ti^{4+} or Zr^{4+} is replaced with trivalent dopants. That is, either TiO$_2$ or ZrO$_2$ layer was doped. The defect reaction governing the addition of trivalent dopants to TiO$_2$ (STO) or ZrO$_2$ (BZO) layer can be expressed in Kröger–Vink notation as:

$$M_2O_3 \xrightarrow{BO_2} 2M'_B + V_O^{\bullet\bullet} + 3O_O^\times \quad (1)$$

where $V_O^{\bullet\bullet}$, B, and M correspond to the oxygen vacancy, B-site cations (either Ti^{4+} or Zr^{4+}) and trivalent dopants (Gd^{3+}), respectively. According to eqn (1), owing to ionic compensation, substitution of two B-site cations with trivalent dopants will result in the formation of one oxygen vacancy. In the supercell approach, the oxygen vacancy formation energy was calculated using

$$E_f = E_{DFT}(vac) - E_{DFT}(ideal) + \sum_i n_i\mu_i + q_{vac}E_F \quad (2)$$

where $E_{DFT}(vac)$ and $E_{DFT}(ideal)$ are respective DFT total energies of the heterostructure with and without an oxygen vacancy defect; n_i is the number of atoms removed; μ_i is the chemical potential of the species removed; q is the charge of the vacancy; and E_F is the Fermi energy. In this work, we are primarily focused on neutral oxygen vacancy defects that are formed to maintain the defect equilibria as given by eqn (1). As a result, the final term in eqn (2) can be essentially neglected. Since only one oxygen is removed in each vacancy calculation, the third term in eqn (2) is calculated as $\frac{1}{2}E_{DFT}(O_2)$, which is the spin polarized total energy (chemical potential) for the ground state of an oxygen molecule in the gas phase. In computing the oxygen chemical potential given in eqn (2), we have neglected important corrections such as oxygen partial pressure, vibrational entropy, and zero-point energy of O$_2$ molecules. The entropic and zero-point energy corrections are essential for making a quantitative comparison with experimental data, which are almost always measured at finite temperatures and specific oxygen partial pressures. Nonetheless, we expect that the relative physical trends in formation energies presented herein are accurately captured since a change in oxygen chemical potential is expected to shift all the formation energies by that value. For instance, for a variety of ABO$_3$ perovskites, Baldassarri *et al.*[80] reported recently that change in the empirical correction factor

for O$_2$ is expected to result in a constant shift of all vacancy formation energies. Overall, we expect that the relative qualitative trends in oxygen vacancy formation energies as a function of interface chemistry and interface location are reliable. Since the calculations presented herein are conducted at 0 K and zero pressure, connecting defect formation data to realistic conditions encountered during the operation of SOFCs would require additional thermodynamic considerations pertaining to defect energetics and concentrations that depend on temperature and oxygen partial pressure.[81] While the operating conditions are simplified and unrealistic in the current approach, the underlying physical principles involved in the calculations offer sufficient physical fidelity in predicting ground state properties of materials, which are foundational to its behavior under real-world conditions. For evaluating the oxygen vacancy formation energy in doped heterostructures, energy minimization was performed where the ionic positions and supercell shape were allowed to fully relax. Throughout the calculations, the volume was held constant at the supercell volume without the oxygen vacancy, which is a reasonable approximation.[60]

3. Results & discussion

3.1 Atomic scale structure and stability of the interface

For the orientation relationship studied in this work, BZO(110)/STO(100) heterostructures can have four different types of interfaces depending on the interface layer chemistries. Fig. 1 depicts energetically and geometrically minimized BaO–SrO, SrO–ZrO$_2$, BaO–TiO$_2$, and ZrO$_2$–TiO$_2$ interfaces. To estimate the stability of the heterostructure formed from two different materials, interface formation energy γ was calculated using

$$\gamma_{interface} = \lim_{N \to \infty} \frac{G_{interface}(N) - N_A G_{bulk,A} - N_B G_{bulk,B}}{A_{interface}} \quad (3)$$

wherein G is the Gibbs free energy (DFT total energy in this case), N is the number of atoms, A is the interface area.[82] The respective interface formation energies for BaO–SrO, SrO–ZrO$_2$, BaO–TiO$_2$, and ZrO$_2$–TiO$_2$ are 12.48 J m^{-2}, 12.10 J m^{-2}, 12.18 J m^{-2}, and 12.04 J m^{-2}, revealing their stable formation. In general, eqn (3) has a factor of 2 for interface formation energy provided that there are two interfaces in the system.[82,83] However, in the present case, due to the presence of the vacuum layer, there is only one interface. In addition, owing to the vacuum layer, there are two surfaces that further contribute to the formation energies presented herein. Since this work is primarily focused on understanding the defect formation at these interfaces, we have neither studied surface effects in detail nor quantified those values. While surface effects are important to understand from a fundamental standpoint, we do not expect them to contribute significantly to the results pertaining to interface defect formation presented in the next sections. Overall, the interface formation energies exhibit that these interfaces are likely to be stable, even more so at experimental conditions that would likely involve higher temperatures for thin film deposition.

In Fig. 2, the heterostructures are shown along the interface normal direction with the relaxed supercells extended in the *x*
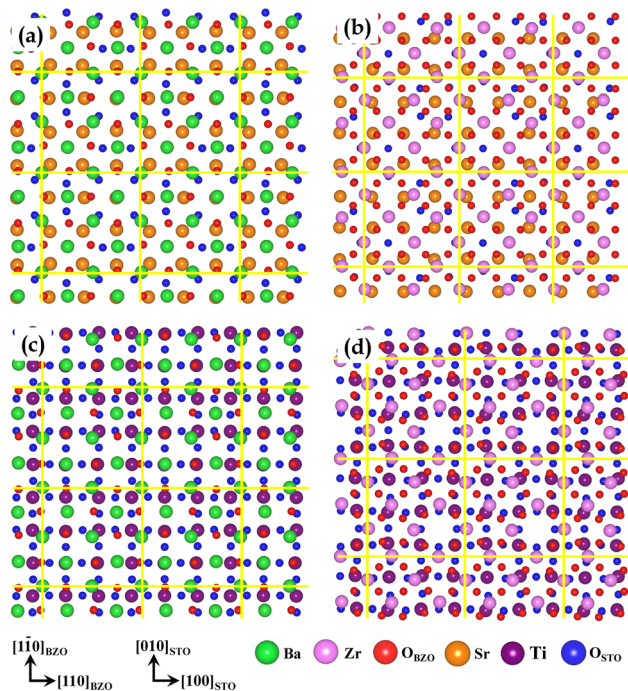
Fig. 2 Top view (normal view) of interface atomic arrangement in the minimized BZO/STO heterostructure shown in Fig. 1 for (a) BaO–SrO (b) ZrO$_2$–SrO (c) BaO–TiO$_2$ and (d) ZrO$_2$–TiO$_2$ interfaces. For clarity, only one atomic layer on each side of the minimized interface is shown for BZO film and STO substrate. The geometrically optimized supercell is extended in the x and y directions (3 × 3) for better visualization, wherein BZO is above STO. The yellow lines (boxed regions) show the misfit dislocation network. The atomic color scheme for metals is same as in Fig. 1. To offer contrast, O$_{BZO}$ and O$_{STO}$ ions are respectively given by red and blue spheres.

Fig. 3 Two locations A and B for oxygen vacancy formation at the interface layers of ideal (undoped) BZO thin film and ideal STO substrate for for (a) BaO–SrO (b) SrO–ZrO$_2$ (c) BaO–TiO$_2$ and (d) ZrO$_2$–TiO$_2$ interfaces. Atomic color scheme and interface orientation relationship is same as in Fig. 2. Red checkered and blue checkered spheres indicate oxygen vacancy locations in BZO and STO, respectively. Only one interface layer of BZO and STO is shown, wherein the view is normal to the interface.

and y direction (3 × 3 × 1) to clearly illustrate the misfit dislocation network, which is indicated *via* yellow lines. We predict that all four interfaces have a dislocation structure with Burgers vector of $\vec{b} = \langle 100 \rangle$, which is somewhat different as compared to misfit dislocations at STO(100)/BZO(100), where the ZrO$_2$–TiO$_2$ interface had a Burgers vector of $\vec{b} = \langle 110 \rangle$.[63] The misfit dislocation spacing between periodic edge dislocations is predicted to be roughly 1.19 nm in both [1$\bar{1}$0]$_{BZO}$ and [110]$_{BZO}$ directions. A common feature uncovered across all the interfaces (Fig. 2) is the presence of electrostatically favorable and unfavorable regions, the latter is often referred to as chemically frustrated regions. Electrostatically favorable regions are where counterions (*i.e.*, anions and cations) from the two sides of the interface are either bonded or are nearest neighbors, whereas chemically frustrated regions are where cation–cation or anion–anion across the interface are nearest neighbors.[58–60] These chemically disparate regions have been shown to influence key material properties across various oxide interfaces.[64] In the following section we discuss how these regions influence oxygen vacancy formation at BZO(110)/STO(100) interfaces.

3.2 Oxygen vacancy formation in ideal heterostructures

In ideal (undoped) heterostructures, for each interface, we studied oxygen vacancy formation at two locations **A** and **B**
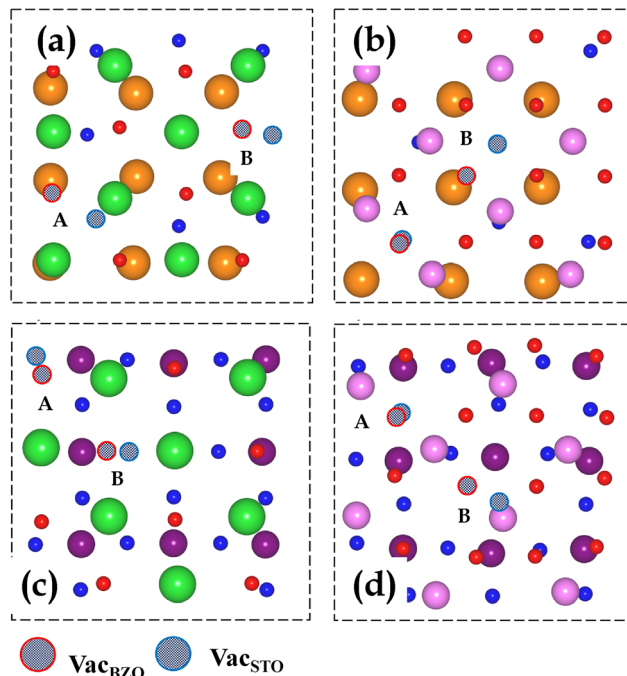
shown in Fig. 3. Vacancy sites were chosen such that oxygen ions across the interface are in close proximity. The rationale for this choice is that such chemically frustrated locations at oxide interfaces are expected to exhibit low vacancy formation energy because of the repulsive Coulombic force between anions. Fig. 4 depicts oxygen vacancy formation energies for the four undoped
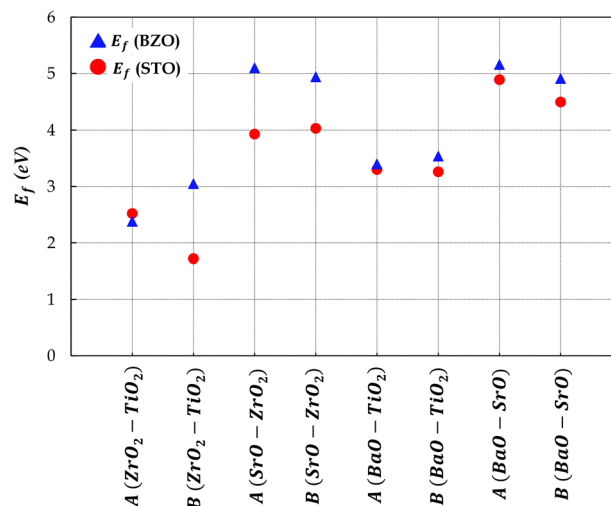

Fig. 4 Vacancy formation energies (E_f) in ideal BZO/STO heterostructures for various interface terminations. Vacancy sites A and B are shown in Fig. 3.

interfaces at sites **A** and **B** revealing that ZrO_2–TiO_2 interface exhibits the lowest formation energy either in ZrO_2 or in TiO_2 side of the interface. The highest formation energies are uncovered for BaO–SrO interface, whereas SrO–ZrO_2 and BaO–TiO_2 interfaces demonstrate energies somewhere in the middle. Since oxygen density is greatest in the ZrO_2–TiO_2 interface, removing an oxygen ion from the chemically frustrated region is energetically favorable as compared to BaO–SrO interface, which has the lowest oxygen density. Across all the four interfaces, oxygen vacancy formation is energetically favorable in the STO side of the interface.

3.3 Oxygen vacancy formation in doped heterostructures

To study the role of dopants and resulting oxygen vacancy formation due to charge neutrality (eqn (1)), we studied oxygen vacancy formation at several sites in doped ZrO_2–TiO_2, ZrO_2–SrO, and BaO–TiO_2 interfaces. Vacancy sites were chosen as representative cases of dissimilar nearest neighbor environment at the three interfaces. Depicted in Fig. 5, vacancy sites are given by numbers **1**–**14**, with respective energies for these numbered sites and their location with respect to the two gadolinium dopants given in Table 1. Since acceptor doping was strictly performed on B-site cations, vacancies were studied in the interface layer of both ZrO_2 and TiO_2 at the ZrO_2–TiO_2 interface, whereas in SrO–ZrO_2 and BaO–TiO_2 interfaces, vacancies were studied in the interface ZrO_2 and TiO_2 layers, respectively. Depending on the location of the two trivalent dopants, the oxygen vacancies can form at first nearest-neighbor (1NN) or second nearest-neighbor (2NN) distance or a combination of these two (1NN and 2NN). We restricted our calculations to first and second neighbors as it has been reported for other oxides that formation of oxygen vacancies is most stable at 1NN and 2NN distances and the influence of dopants diminishes at and beyond 3NN.[84]

Among the various oxygen vacancy sites studied (Table 1), site **4** on the TiO_2 layer of the ZrO_2–TiO_2 interface is predicted to be the lowest energy site, which has two dopants at 1NN–2NN. Since site **4** is situated in the vicinity to two oxygen ions located in the ZrO_2 layer, oxygen removal at this site is predicted to be spontaneous. That is, the removal of oxygen ions

Table 1 Oxygen vacancy formation energies (E_f) in doped BZO/STO heterostructures for various interface terminations. Corresponding numbered vacancy sites are depicted in Fig. 5. Location of the two dopants are given via nearest neighbor (NN) distance with respect to the vacancy. location different dopant arrangements for the same oxygen vacancy site are given by "a" and "b"

Interface	Vacancy site	Defect-dopant cluster location		E_f (eV)
ZrO_2–TiO_2	**1**	ZrO_2	1NN–2NN	0.65
	2		1NN–1NN	−0.53
	3a		1NN–2NN	−1.31
	3b		1NN–1NN	−1.74
	4	TiO_2	1NN–2NN	−2.05
	5		1NN–1NN	−0.74
SrO–ZrO_2	**6a**	ZrO_2	2NN–2NN	0.96
	6b		1NN–1NN	0.94
	7		1NN–2NN	1.52
	8a		1NN–2NN	0.50
	8b		1NN–1NN	0.54
BaO–TiO_2	**9**	TiO_2	2NN–2NN	−1.01
	10		1NN–2NN	−1.05
	11		1NN–1NN	1.27
	12a		2NN–2NN	−0.86
	12b		1NN–2NN	0.42
	13		1NN–2NN	0.13
	14		1NN–1NN	0.91

from oxygen rich environment is exothermic due to unfavorable electrostatic interactions across the interface. Site **1** located on the ZrO_2 side of the interface sits right above a titanium ion, resulting in endothermic (positive) vacancy formation energy since removal of oxygen from a stable electrostatic region is energetically costly. At the ZrO_2–TiO_2 interface, excluding site **1**, which demonstrates endothermic formation energy, vacancy sites **2**, **3**, **4**, and **5** exhibit exothermic (negative) formation energies. Significant energy differences are observed between the dissimilar dopant arrangements at different sites and in some cases, even for the same site. For instance, sites **3a** and **3b** having respective dopant arrangements of 1NN–2NN and 1NN–1NN exhibit an energy difference of −0.42 eV. We predict that the binding of oxygen vacancies with dopants for a given case would vary depending on the precise location of dopants and oxygen defects, which can be attributed to the interface atomic relaxation and dissimilar NN environment encountered at the interface.
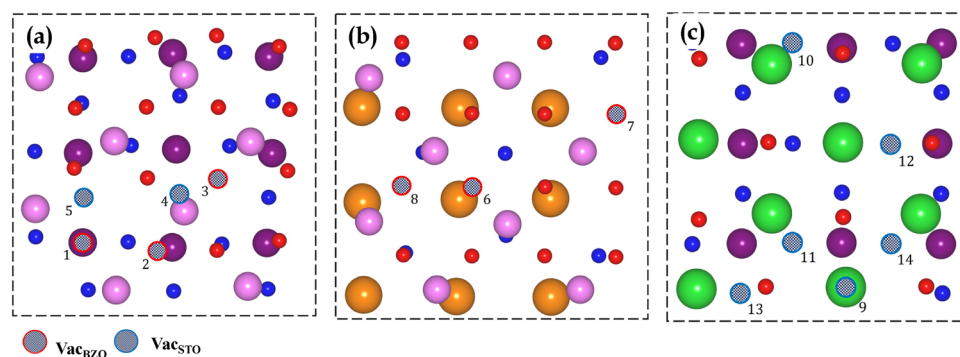

Fig. 5 Locations given by numbers for oxygen vacancy formation at the interface layers of doped BZO thin film and doped STO substrate for (a) ZrO_2–TiO_2 (b) ZrO_2–SrO and (c) BaO–TiO_2 interfaces. Atomic color scheme and interface orientation relationship is same as in Fig. 3. Only one interface layer of BZO and STO is shown, wherein the view is normal to the interface.

A contrasting picture is however uncovered at the SrO–ZrO$_2$ interface. Vacancy sites **6**, **7**, and **8** examined at this interface exhibit endothermic vacancy formation. The basic reason for this behavior is that these vacancy sites on the ZrO$_2$ side are located in a region of stable electrostatic interaction resulting in endothermic formation energies. For instance, site **8** is very close to the dislocation line, but is located in a region where there are no additional oxygen ions from either side of the interface. Removal of oxygen at this site would result in a local environment that is oxygen poor leaving neighboring metal ions with a smaller number of counterions resulting in their undercoordination. At vacancy sites **6** and **8** (sites are distinguished by notation **6a**, **6b**, **8a**, and **8b**), dissimilar dopant arrangements such as 1NN–1NN, 1NN–2NN, and 2NN–2NN resulted in minor differences in formation energies. This outcome emphasizes that dopant arrangement would have minimal influence on vacancy formation energies at the SrO–ZrO$_2$ interface. That is, vacancy formation energy would be primarily governed by its location at the interface with marginal influence from the neighboring dopant arrangement.

A different story unfolds at the BaO–TiO$_2$ interface, wherein a mix of exothermic and endothermic formation energies are uncovered. Vacancy sites **9**, **10**, and **12a** exhibit exothermic vacancy formation, whereas sites **11**, **12b**, **13** and **14** demonstrate endothermic vacancy formation. As observed before, the main reason is the specific vacancy location. However, contrasting behavior is observed as compared to ZrO$_2$–TiO$_2$ and SrO–ZrO$_2$ interfaces. For instance, vacancy site **9**, wherein the oxygen ion is located on top of the larger Ba ion is exothermic. This site is comparable in nearest neighbor environment with vacancy sites **1** and **6** in SrO–ZrO$_2$ and SrO–ZrO$_2$ interfaces, respectively, both of which are endothermic. Since this region is electrostatically stable due to counterions bonded to each other, one would expect endothermic vacancy formation at site **9**, similar to that observed at sites **1** and **6**. However, at BaO–TiO$_2$ interface, since the Ba ion is very large, the removal of oxygen ion decreases the strain at the interface, which facilitates exothermic vacancy formation. Similar behavior is uncovered at vacancy site **10**. Nonetheless, vacancy sites **11**, **13**, and **14** exhibit endothermic vacancy formation because removal of oxygen ion from regions where they are not directly bonded with larger Ba ions requires greater energy.

We further investigated this behavior to comprehend the fundamental factors that result in dissimilarities and commonalities among the various BZO/STO interfaces and how vacancy formation is influenced not only by the vacancy location, but also by the interface layer chemistry and nearest neighbor dopant arrangement. To this end, for vacancy site **A** shown in Fig. 3, we computed oxygen vacancy formation for ZrO$_2$–TiO$_2$, SrO–ZrO$_2$, and BaO–TiO$_2$ interfaces for dissimilar dopant arrangements, which is given in Table 2. Across the three aforementioned interfaces, since vacancy site **A** has similar nearest neighbor environment involving unfavorable anion–anion electrostatic interactions or the so-called chemically frustrated regions, this approach will allow us to distinguish the role of basic factors governing vacancy formation. For instance, we would expect that

Table 2 For three different interfaces, oxygen vacancy formation energies (E_f) in doped BZO/STO heterostructures with various dopant arrangements for oxygen vacancy at site A, which is shown in Fig. 3

Interface	Dopant location	Dopant position	E_f (eV)
ZrO$_2$–TiO$_2$	TiO$_2$	1NN–1NN	−0.20
ZrO$_2$–TiO$_2$	TiO$_2$	2NN–2NN	−1.11
ZrO$_2$–TiO$_2$	ZrO$_2$	1NN–1NN	−0.47
ZrO$_2$–TiO$_2$	ZrO$_2$	2NN–2NN	−0.67
SrO–ZrO$_2$	ZrO$_2$	1NN–1NN	0.36
BaO–TiO$_2$	TiO$_2$	1NN–1NN	1.30
BaO–TiO$_2$	TiO$_2$	1NN–2NN	−1.01

oxygen vacancy formation at site **A** in the neighborhood of dopants in chemically frustrated regions would be exothermic since the removal of oxygen from a repulsive interaction will be energetically favorable. This is observed at ZrO$_2$–TiO$_2$ interface, wherein higher density of oxygen ions and repulsive anion–anion interactions result in exothermic vacancy formation for 1NN–1NN and 2NN–2NN dopant configurations, both in ZrO$_2$ and TiO$_2$ layers (Table 2). On the contrary, at SrO–ZrO$_2$ and BaO–TiO$_2$ interfaces, endothermic oxygen vacancy formation is uncovered for 1NN–1NN dopant arrangement, revealing that the presence of larger trivalent dopants at 1NN along with larger Sr or Ba ions at the interface creates enough strain to raise the system energy and result in endothermic formation tendencies. In addition, at BaO–TiO$_2$ interface, in contrast to endothermic formation energy for 1NN–1NN dopant arrangement, 1NN–2NN yields exothermic vacancy formation because one of the larger dopants is moved further from the defect location reducing the strain. Overall, these results reveal that in addition to the precise location at the interface, the nearest neighbor environment, the interface layer chemistry, and the dopant arrangements are critical in governing oxygen vacancy formation at mismatched BZO/STO interfaces.

These findings demonstrate a broad range of oxygen vacancy formation energies at BZO/STO interfaces that are contingent on a combination of factors that include nearest neighbor environment and interface layer chemistry. These results shed light on the complexity associated with disentangling the fundamental aspects of oxygen vacancy formation at mismatched oxide interfaces, which is noticeably different than that observed in the grain interior.[60] It is likely that the actual scenario is even more complex at oxide heterointerfaces, specifically due to factors such as strain, temperature, oxygen partial pressure, and dopant segregation, which could further influence the vacancy formation energies. Such complex behavior has been observed in other oxide heterostructures[60] and reveals that STO/BZO heterostructures are likely to have a notable fraction of oxygen vacancies, considering that several locations on either side of the interface display exothermic vacancy formation energies. In addition, present calculations are performed at 0 K, revealing that at higher temperatures and in experimental conditions, a higher oxygen vacancy fraction is expected at such mismatched oxide heterostructures. It is worth noting that calculations herein are conducted for dilute fraction of dopants and defects. At higher fractions, formation of oxygen vacancy at a given location is likely to impact the formation energies of additional vacancies in the neighborhood owing to

vacancy–vacancy and vacancy–dopant interactions.[59] Addressing the complexity associated with higher defect concentration would require large supercells and demand high computational resources, both of which are beyond the scope of this work. Nonetheless, these results make a compelling case to pursue such work in the future. In general, results herein underpin the complexity involved in understanding defect behavior at mismatched oxide heterointerfaces,[64] further revealing that studying oxygen vacancy formation at such interfaces is a fundamental prerequisite to identify ionic transport mechanisms in thin film oxide electrolytes.

3.4 Electronic structure and charge transfer

Detailed density of states (DOS) analysis was performed to gain insights into the electronic structure of the material and study the electron occupancies below and above the Fermi level. In all cases, Fermi level is set to 0 eV, so states with negative and positive energies indicate occupied and unoccupied (virtual) orbitals, respectively. To interpret the influence of dissimilar interfaces and resulting disparate bonding on the electronic structure, we studied the total DOS for BaO–SrO, BaO–TiO$_2$, SrO–ZrO$_2$, and ZrO$_2$–TiO$_2$ interfaces, which is shown in Fig. 6(a), whereas Fig. 6(b) shows amplification of DOS at and around the Fermi level. Evidently, the DOS for various interfaces exhibit similar features around the Fermi level and comparable band gaps. Nonetheless, the BaO–TiO$_2$ interface shows occupancies in the band gap, primarily due to the partially filled Ti 3d states. To further provide a detailed view of the electronic structure, DOS were projected on the Sr, Ti, O, Ba, and Zr ions and their respective orbitals. Fig. 6(c)–(f) offers projected DOS for BaO–SrO, BaO–TiO$_2$, SrO–ZrO$_2$, and ZrO$_2$–TiO$_2$ interfaces, respectively. Predominant
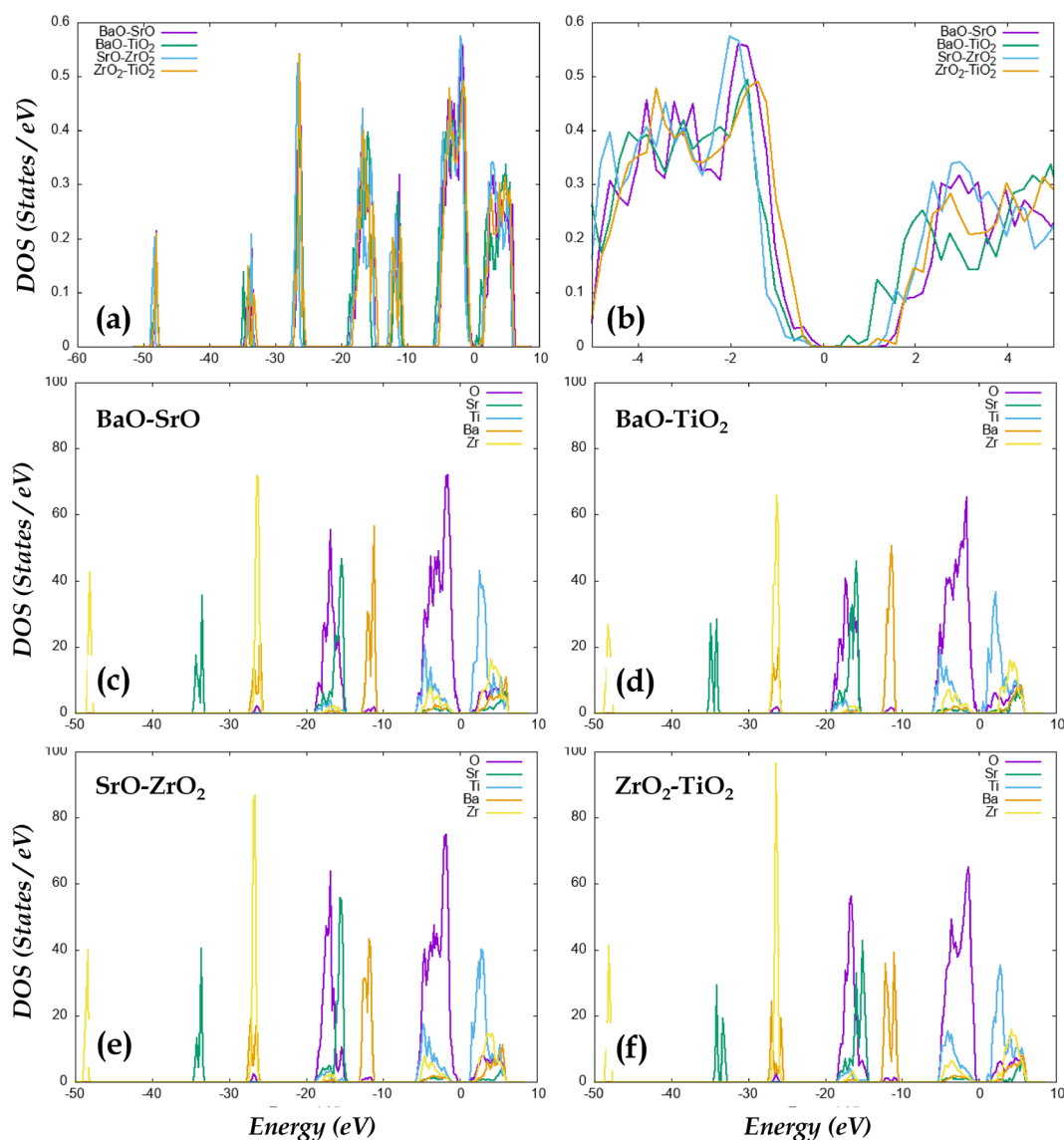

Fig. 6 For BZO/STO heterostructures, (a) total electronic density of states (DOS) for the four interfaces and (b) zoomed region in total DOS around the band gap. Partial DOS projected onto Ba, Zr, O, Sr, and Ti atoms in (c) BaO−SrO (d) BaO−TiO$_2$ (e) SrO−ZrO$_2$ and (f) ZrO$_2$−TiO$_2$ interfaces. Only spin-up channel is shown. In all cases, the Fermi level is shifted to 0 eV.

contribution to the valence band in these interfaces comes from O, with somewhat noticeable contribution from Ti and minor contributions from Ba, Sr, and Zr ions. The conduction band primarily contains contribution from Ti along with noticeable presence of Zr, as well as minor contributions from O, Ba, and Sr atoms. The overlap of various orbital signatures from different species in the valence band reveal strong interfacial chemical bonding, which is evident in interface stability analysis and interface formation energies reported earlier. Ti^{3+} defect states are likely to be observed in reducing environment, wherein an oxygen vacancy is formed in the neighborhood, which has two electrons associated with the vacant site.[85] These two electrons are often trapped by neighboring Ti^{4+} ions, reducing them to Ti^{3+}. As evident from Fig. 6, at the BaO–TiO$_2$ interface, Ti^{3+} polarized states appear within the band gap, which offers the possibility of introducing electron conductivity in the material. However, since the main function of thin film oxide electrolyte is high ionic conductivity, presence of electronic conductivity in the electrolyte could create an internal short and result in a voltage drop, which is detrimental to the overall performance of the SOFCs. At the BaO–TiO$_2$ interface, since oxygen vacancy formation is exothermic in some cases, it is likely that this interface would exhibit Ti^{3+} polarized states. These results reveal that for designing thin film electrolytes for SOFC using the BZO/STO heterostructures, BaO–TiO$_2$ interface should be avoided.

In ZrO$_2$–TiO$_2$, BaO–TiO$_2$, and SrO–ZrO$_2$ interfaces, we further compared DOS before and after the inclusion of oxygen vacancies and corresponding dopants to study the modifications in the electronic states near the Fermi level. This analysis was limited to most favorable oxygen vacancy formation in ease case. For instance, DOS for ideal ZrO$_2$–TiO$_2$ interface with vacancy defect on either side is given in Fig. 7(a) and DOS for doped ZrO$_2$–TiO$_2$ interface with vacancy defect on either side is offered in Fig. 7(b). For the undoped (ideal) case (Fig. 7(a)), while slightly higher occupancies are observed in the case of oxygen vacancy in TiO$_2$ side of the interface, the overall features for both the cases are more or less similar. For the doped case (Fig. 7(b)), similar behavior is observed indicating that these ZrO$_2$–TiO$_2$ interface easily accommodates oxygen vacancy defects with and without dopants. Although we have not shown the DOS plots for the ideal BaO–TiO$_2$ and SrO–ZrO$_2$ interfaces, analogous to the ZrO$_2$–TiO$_2$ interface, doped BaO–TiO$_2$ and SrO–ZrO$_2$, interfaces (Fig. 7(c)) do not demonstrate any remarkable changes in DOS features when compared to the undoped cases. One fundamental difference is that the formation energies in doped ZrO$_2$–TiO$_2$ and BaO–TiO$_2$ interfaces are exothermic (Table 1), whereas those in corresponding undoped cases are endothermic (Fig. 4). In contrast, for the SrO–ZrO$_2$ interfaces, formation energies at both the undoped and the doped cases are endothermic, which indicates that doping is likely to allow for facile vacancy formation at ZrO$_2$–TiO$_2$ and BaO–TiO$_2$.

To examine the charge redistribution and interface charge transfer between STO and BZO, charge density differences before and after the charge transfer were computed. The charge density difference ($\Delta\rho$) was computed using

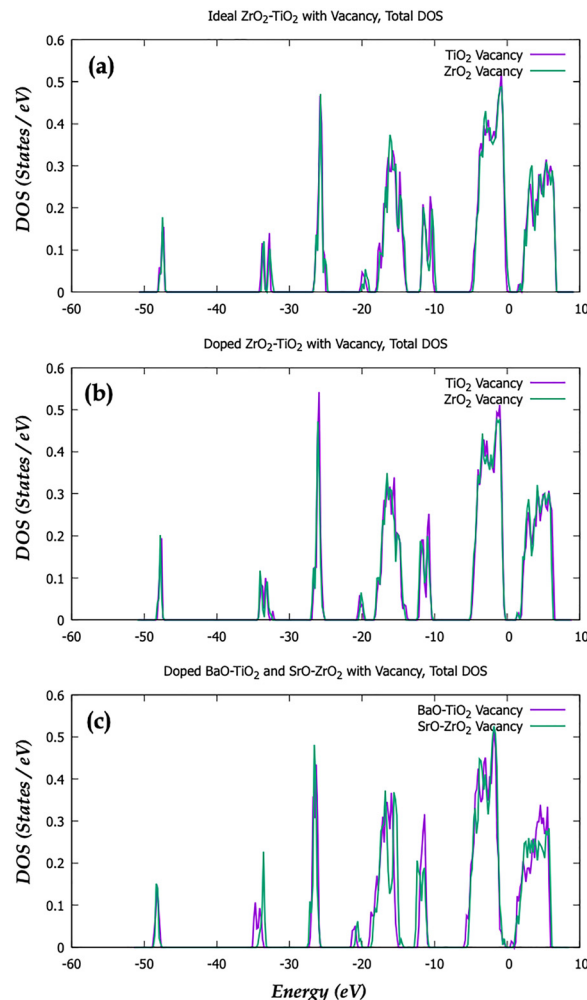$$\Delta\rho = \rho_{(BZO/STO)} - \rho_{(BZO)} - \rho_{(STO)} \quad (4)$$

Fig. 7 Total DOS for (a) ideal ZrO$_2$–TiO$_2$ interface with vacancy defect on either side and (b) doped ZrO$_2$–TiO$_2$ interface with vacancy defect on either side. (c) Total DOS for vacancy defects in doped BaO–TiO$_2$ and SrO–ZrO$_2$ interfaces. Only spin-up channel is shown. In all cases, the Fermi level is shifted to 0 eV.

where $\rho_{(BZO/STO)}$, $\rho_{(BZO)}$, and $\rho_{(STO)}$ correspond to the charge density of the BZO/STO heterostructure, isolated BZO, and isolated STO, respectively. In this formalism, $\Delta\rho$ demonstrates the charge density variations in STO and BZO when they are brought in contact. For the case of heterostructure with dopants and defects, various terms in eqn (4) were modified accordingly. For the heterostructures in their ground state (Fig. 8), while a common trend of charge transfer from BZO to STO is observed, the qualitative features of charge density difference exhibit some dissimilarity. That is, in BaO–SrO (Fig. 8(a)) and SrO–ZrO$_2$ (Fig. 8(b)) interfaces, charge has entirely migrated to the STO structure, whereas in BaO–TiO$_2$ (Fig. 8(c)) and ZrO$_2$–TiO$_2$ (Fig. 8(d)) interfaces, charge accumulation reaches as far as the oxygen atoms in the second row of STO. The observed fundamental trend of charge transfer from BZO to STO is further corroborated in the 2D difference charge density slices given below the respective 3D plots in Fig. 8. Using this strategy, we can elucidate charge migration at the interface guided by various defects. To this end, Fig. S1 offers top views of charge
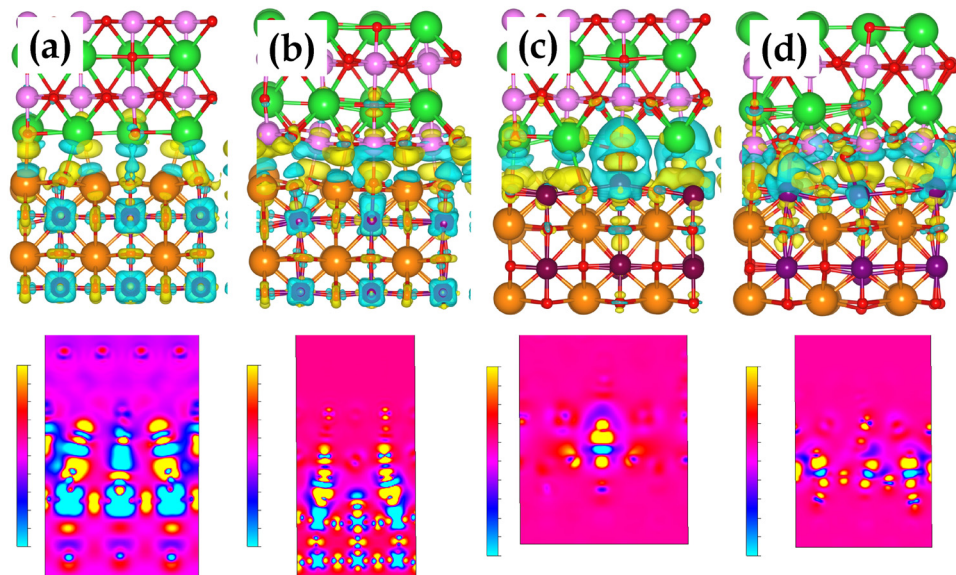
Fig. 8 For BZO/STO heterostructure, three-dimensional (top panel) and two-dimensional (bottom panel) charge density difference plots for (a) BaO–SrO (b) ZrO_2–SrO (c) BaO–TiO_2 and (d) ZrO_2–TiO_2 interfaces. Atomic color scheme is same as in Fig. 1. Yellow and cyan isosurfaces indicate regions of charge accumulation and depletion, respectively. The isosurface value is 0.2×10^{-2} e Å^{-3}.

density difference for select few cases. Depicted in Fig. S1a is the charge density difference for the ideal ZrO_2–TiO_2 interface, *i.e.*, without vacancies or dopants. When compared with vacancy and dopants on the TiO_2 side for the most stable location (Fig. S1b) and with vacancy and dopants on the ZrO_2 side for the most stable location (Fig. S1c), basic difference can be deduced. For defects on the TiO_2 side, the dopant atom in the center has accumulated charge from the hole. Overall, the charge difference is more grouped together by atoms, wherein the dopants and vacancy have greater charge distributions on the TiO_2 side. For ZrO_2–TiO_2 interface, the vicinity of misfit dislocation has created extra charge depletion around oxygen atoms on the TiO_2 side of the interface, allowing their removal to be energetically favorable. For defects on the ZrO_2 side, a qualitatively similar charge distribution profile is uncovered. For the BaO–TiO_2 interface, given in Fig. S1d and e is the charge density difference for the ideal and that with vacancy and dopants on the TiO_2 side for the most stable location, respectively. For the ideal case, it is evident that charges are localized at certain locations near the interface from an oxygen vacancy that could potential be placed near the dopants that formed with high stability. This location is identified as the one that is on the misfit dislocation line, which offers opportunities for vacancies to form spontaneously. From the charge density difference in the doped heterostructure, the large clusters have now distributed charge, granting higher occupancies for both sides of the interface. Overall, in all cases with defects, a general trend of charge transfer from BZO to STO is observed, which is consistent with the ideal cases.

heterostructures and predicted the atomic scale structure of misfit dislocations. Overall, we have found that BaO–SrO, SrO–ZrO_2, BaO–TiO_2, and ZrO_2–TiO_2 interfaces are thermodynamically stable. A periodic misfit dislocation pattern is uncovered for all possible interface terminations. To understand the fundamental role of interface layer chemistry, formation energies of oxygen vacancy defects were determined. Across all the four interfaces, oxygen vacancy formation is energetically favorable in $SrTiO_3$ side of the interface in ideal heterostructures. In heterostructures with oxygen vacancy defects and trivalent dopants, we found that in addition to the precise location at the interface, the nearest neighbor environment, the interface layer chemistry, and the dopant arrangements are critical in governing oxygen vacancy formation. Exothermic and endothermic oxygen vacancy formation energies are uncovered, with the former primarily associated with chemically frustrated regions. The charge transfer mechanism from $BaZrO_3$ to $SrTiO_3$ is observed for both defect-free and defective interfaces. Fundamental insights offered in this work highlight the importance of understanding the atomic and electronic structure of oxide interfaces and correlating it with oxygen vacancy defect formation, which is critical in evaluating ionic transport in solid oxide fuel cell electrolytes based on oxide thin films.

4. Conclusions

Using first principles density functional theory, we investigated the thermodynamic stability of $BaZrO_3(110)/SrTiO_3(100)$

Author contributions

P. P. D. conceptualized the study and supervised J. R., who performed all the calculations. J. R. and P. P. D. wrote the initial draft of the manuscript. Both the authors discussed and provided input on writing the final version of the manuscript.

Conflicts of interest

There are no conflicts to declare.

Data availability

The majority of the data generated and analyzed in this work are included in this article. Additional data and scripts that support the findings of this work are available from the corresponding author upon reasonable request.

Supporting information: charge density difference in BZO/STO heterostructures for different interface chemistry. See DOI: https://doi.org/10.1039/d5ya00220f.

Acknowledgements

References

1 P. Zubko, S. Gariglio, M. Gabay, P. Ghosez and J.-M. Triscone, Interface Physics in Complex Oxide Heterostructures, *Annu. Rev. Condens. Matter Phys.*, 2011, **2**, 141.

2 J. A. Sulpizio, S. Ilani, P. Irvin and J. Levy, Nanoscale Phenomena in Oxide Heterostructures, *Annu. Rev. Mater. Res.*, 2014, **44**, 117.

3 N. Pryds and V. Esposito, When Two Become One: An Insight into 2D Conductive Oxide Interfaces, *J. Electroceram.*, 2017, **38**, 1.

4 P. Yu, Y.-H. Chu and R. Ramesh, Oxide Interfaces: Pathways to Novel Phenomena, *Mater. Today*, 2012, **15**, 320.

5 Z. Huang, Ariando, X. R. Wang, A. Rusydi, J. Chen, H. Yang and T. Venkatesan, Interface Engineering and Emergent Phenomena in Oxide Heterostructures, *Adv. Mater.*, 2018, **30**, 1802439.

6 H. Y. Hwang, Y. Iwasa, M. Kawasaki, B. Keimer, N. Nagaosa and Y. Tokura, Emergent Phenomena at Oxide Interfaces, *Nat. Mater.*, 2012, **11**, 103.

7 J. A. Kilner and M. Burriel, Materials for Intermediate-Temperature Solid-Oxide Fuel Cells, *Annu. Rev. Mater. Res.*, 2014, **44**, 365–393.

8 E. Fabbri, D. Pergolesi and E. Traversa, Ionic Conductivity in Oxide Heterostructures: The Role of Interfaces, *Sci. Technol. Adv. Mater.*, 2010, **11**, 054503.

9 K. E. Sickafus, R. W. Grimes, J. A. Valdez, A. Cleave, M. Tang, M. Ishimaru, S. M. Corish, C. R. Stanek and B. P. Uberuaga, Radiation-induced Amorphization Resistance and Radiation Tolerance in Structurally Related Oxides, *Nat. Mater.*, 2007, **6**, 217–223.

10 M. Salluzzo, S. Gariglio, D. Stornaiuolo, V. Sessi, S. Rusponi, C. Piamonteze, G. M. De Luca, M. Minola, D. Marré, A. Gadaleta, H. Brune, F. Nolting, N. B. Brookes and G. Ghiringhelli, Origin of Interface Magnetism in $BiMnO_3/SrTiO_3$ and $LaAlO_3/SrTiO_3$ Heterostructures, *Phys. Rev. Lett.*, 2013, **111**, 087204.

11 B. Zhu, L. Fan and P. Lund, Breakthrough Fuel Cell Technology Using Ceria-based Multi-functional Nanocomposites, *Appl. Energy*, 2013, **106**, 163–175.

12 J. Wang, G. Ji, Y. Liu, M. A. Gondal and X. Chang, Cu_2O/TiO_2 Heterostructure Nanotube Arrays Prepared by an Electrodeposition Method Exhibiting Enhanced Photocatalytic Activity for CO_2 Reduction to Methanol, *Catal. Commun.*, 2014, **46**, 17–21.

13 B. C. H. Steele and A. Heinzel, Materials for Fuel-cell Technologies, *Nature*, 2001, **414**, 345.

14 A. Boudghene Stambouli and E. Traversa, Solid Oxide Fuel Cells (SOFCs): A Review of an Environmentally Clean and Efficient Source of Energy, *Renewable Sustainable Energy Rev.*, 2002, **6**, 433.

15 S. C. Singhal and K. Kendall, *High-temperature Solid Oxide Fuel Cells: Fundamentals, Design and Applications*, Elsevier, Oxford, 2003.

16 E. D. Wachsman and K. T. Lee, Lowering the Temperature of Solid Oxide Fuel Cells, *Science*, 2011, **334**, 935.

17 A. Jaiswal, A. Pesaran, S. Omar and E. D. Wachsman, Ceria/Bismuth Oxide Bilayer Electrolyte Based Low-Temperature SOFCs with Stable Electrochemical Performance, *ECS Trans.*, 2017, **78**, 361.

18 J. Santiso, J. Roqueta, N. Bagués, C. Frontera, Z. Konstantinovic, Q. Lu, B. Yildiz, B. Martínez, A. Pomar, L. Balcells and F. Sandiumenge, Self-Arranged Misfit Dislocation Network Formation upon Strain Release in $La_{0.7}Sr_{0.3}MnO_3/LaAlO_3(100)$ Epitaxial Films under Compressive Strain, *ACS Appl. Mater. Interfaces*, 2016, **8**, 16823–16832.

19 C. Korte, A. Peters, J. Janek, D. Hesse and N. Zakharov, Ionic conductivity and activation energy for oxygen ion transport in superlattices—the semicoherent multilayer system YSZ-(ZrO_2 + 9.5 mol% Y_2O_3)/Y_2O_3, *Phys. Chem. Chem. Phys.*, 2008, **10**, 4623–4635.

20 G. F. Harrington, A. Cavallaro, D. W. McComb, S. J. Skinner and J. A. Kilner, The Effects of Lattice Strain, Dislocations, and Microstructure on the Transport Properties of YSZ Films, *Phys. Chem. Chem. Phys.*, 2017, **19**, 14319–14336.

21 D. Choudhury, B. Pal, A. Sharma, S. V. Bhat and D. D. Sarma, Magnetization in Electron- and Mn-doped $SrTiO_3$, *Sci. Rep.*, 2013, **3**, 1433.

22 R. A. Maier and C. A. Randall, Low-Temperature Ionic Conductivity of an Acceptor-Doped Perovskite: I. Impedance of Single-Crystal $SrTiO_3$, *J. Am. Ceram. Soc.*, 2016, **99**(10), 3350–3359.

23 J. Cheng, Y. Wang, J. Luo and K. Yang, δ-Doping Effects on Electronic and Energetic Properties of $LaAlO_3/SrTiO_3$ Heterostructure: First-Principles Analysis of 23 Transition-Metal Dopants, *Adv. Mater. Interfaces*, 2017, **4**, 1700579.

24 E. W. McFarland and H. Metiu, Catalysis by Doped Oxides, *Chem. Rev.*, 2013, **113**, 4391–4427.

25 Y. Pai, A. Tylan-Tyler, P. Irvin and J. Levy, Physics of SrTiO₃-based Heterostructures and Nanostructures: A Review, *Rep. Prog. Phys.*, 2018, **81**, 036503.

26 W. Luo, W. Duan, S. G. Louie and M. L. Cohen, Structural and Electronic Properties of n-doped and p-doped SrTiO₃, *Phys. Rev. B: Condens. Matter Mater. Phys.*, 2004, **70**, 214109.

27 P. C. Bowes, J. N. Baker and D. L. Irving, Survey of acceptor dopants in SrTiO₃: Factors limiting room temperature hole concentration, *J. Am. Ceram. Soc.*, 2020, **103**, 1156–11733.

28 C. Y. R. Vera, H. Ding, D. Peterson, W. T. Gibbons, M. Zhou and D. Ding, A mini-review on proton conduction of BaZrO3-based perovskite electrolytes, *J. Phys. Energy*, 2021, **3**, 032019.

29 P. P. Dholabhai, E. Martinez and B. P. Uberuaga, Influence of Chemistry and Misfit Dislocation Structure on Dopant Segregation at Complex Oxide Heterointerfaces, *Adv. Theory Simul.*, 2019, **2**, 1800095.

30 S. Hui and A. Petric, Electrical Properties of Yttrium-Doped Strontium Titanate under Reducing Conditions, *J. Electrochem. Soc.*, 2002, **149**, J1–J10.

31 C. Ohly, S. Hoffmann-Eifert, K. Szot and R. Waser, Electrical Conductivity and Segregation Effects of Doped SrTiO₃ Thin Films, *J. Eur. Ceram. Soc.*, 2001, **21**, 1673–1676.

32 D. V. Azamat, A. G. Badalyan, A. Dejneka, V. A. Trepakov, L. Jastrabik and Z. Frait, High-frequency Electron Paramagnetic Resonance Investigation of Mn³⁺ Centers in SrTiO₃, *J. Phys. Chem. Solids*, 2012, **73**, 822–826.

33 H. Yang, H. S. Lee, P. G. Kotula, Y. Sato, Y. Ikuhara and N. D. Browning, Amphoteric Doping of Praseodymium Pr31 in SrTiO₃ Grain Boundaries, *Appl. Phys. Lett.*, 2015, **106**, 121904.

34 L. Dai, L. Wu, H. Li, H. Hu, Y. Zhuang and K. Liu, Evidence of the Pressure-induced Conductivity Switching of Yttrium-doped SrTiO₃, *J. Phys.: Condens. Matter*, 2016, **28**, 475501.

35 R. Merkle and J. Maier, Defect Association in Acceptor-doped SrTiO₃: Case Study for FeTiVO and MnTiVO, *Phys. Chem. Chem. Phys.*, 2003, **5**, 2297–2303.

36 M. Longo, M. G. S. Costa, A. Z. Simoes, I. L. V. Rosa, C. O. P. Santos, J. Andres, E. Longo and J. A. Varela, On the Photoluminescence Behavior of Samarium-doped Strontium Titanate Nanostructures Under UV Light. A Structural and Electronic Understanding, *Phys. Chem. Chem. Phys.*, 2010, **12**, 7566–7579.

37 E. Gilardi, E. Fabbri, L. Bi, J. L. M. Rupp, T. Lippert, D. Pergolesi and E. Traversa, Effect of Dopant–Host Ionic Radii Mismatch on Acceptor-Doped Barium Zirconate Microstructure and Proton Conductivity, *J. Phys. Chem. C*, 2017, **121**, 9739–9747.

38 D. Han, K. Shinoda, S. Sato, M. Majimad and T. Tetsuya Uda, Correlation between electroconductive and structural properties of proton conductive acceptor-doped barium zirconate, *J. Mater. Chem. A*, 2015, **3**, 1243.

39 W. Lee, J. W. Han, Y. Chen, Z. Cai and B. Yildiz, Cation Size Mismatch and Charge Interactions Drive Dopant Segregation at the Surfaces of Manganite Perovskites, *J. Am. Chem. Soc.*, 2013, **135**, 7909–7925.

40 M. Shirpour, B. Rahmati, W. Sigle, P. A. van Aken, R. Merkle and J. Maier, Dopant Segregation and Space Charge Effects in Proton-Conducting BaZrO₃ Perovskites, *J. Phys. Chem. C*, 2012, **116**, 2453–2461.

41 S. Chung, S. L. Kang and V. P. Dravid, Effect of Sintering Atmosphere on Grain Boundary Segregation and Grain Growth in Niobium-Doped SrTiO₃, *J. Am. Ceram. Soc.*, 2002, **85**, 2805–2810.

42 R. B. Wexler, G. S. Gautam, E. B. Stechel and E. A. Carter, Factors Governing Oxygen Vacancy Formation in Oxide Perovskites, *J. Am. Chem. Soc.*, 2021, **143**, 13212–13227.

43 Q. Yang, J. X. Cao, Y. Ma, Y. C. Zhou, L. M. Jiang and X. L. Zhong, Strain effects on formation and migration energies of oxygen vacancy in perovskite ferroelectrics: A first-principles study, *J. Appl. Phys.*, 2013, **113**, 184110.

44 R. Merkle, Y. A. Mastrikov, E. A. Kotomin, M. M. Kuklja and J. Maier, First Principles Calculations of Oxygen Vacancy Formation and Migration in Ba₁₋ₓSrₓCo₁₋ᵧFeᵧO₃₋δ Perovskites, *J. Electrochem. Soc.*, 2012, **159**, B219–B226.

45 I. Kagomiya, K. Jimbo, K. Kakimoto, M. Nakayama and O. Masson, Oxygen vacancy formation and the ion migration mechanism in layered perovskite (Sr,La)₃Fe₂O₇, *Phys. Chem. Chem. Phys.*, 2014, **16**, 10875.

46 J. M. Börgers and R. A. De Souza, The surprisingly high activation barrier for oxygen-vacancy migration in oxygen-excess manganite perovskites, *Phys. Chem. Chem. Phys.*, 2020, **22**, 14329.

47 L. Zhang, B. Liu, H. Zhuang, P. R. C. Kent, V. R. Cooper, P. Ganesh and H. Xu, Oxygen vacancy diffusion in bulk SrTiO3 from density functional theory calculations, *Comput. Mater. Sci.*, 2016, **118**, 309–315.

48 J. J. Brown, Z. Ke, W. Geng and A. J. Page, Oxygen Vacancy Defect Migration in Titanate Perovskite Surfaces: Effect of the A-Site Cations, *J. Phys. Chem. C*, 2018, **122**, 14590–14597.

49 M. Cherry, M. S. Islam and C. R. A. Catlow, Oxygen Ion Migration in Perovskite-Type Oxides, *J. Solid State Chem.*, 1995, **118**, 125.

50 Y. Pai, A. Tylan-Tyler, P. Irvin and J. Levy, Physics of SrTiO₃-based Heterostructures and Nanostructures: A Review, *Rep. Prog. Phys.*, 2018, **81**, 036503.

51 M. Sillassen, P. Eklund, N. Pryds, E. Johnson, U. Helmersson and J. Bøttiger, Low-temperature Superionic Conductivity in Strained Yttria-stabilized Zirconia, *Adv. Funct. Mater.*, 2010, **20**, 2071–2076.

52 J. Garcia-Barriocanal, A. Rivera-Calzada, M. Varela, Z. Sefrioui, E. Iborra, C. Leon, S. J. Pennycook and J. Santamaria, Colossal Ionic Conductivity at Interfaces of Epitaxial ZrO₂:Y₂O₃/SrTiO₃ Heterostructures, *Science*, 2008, **321**, 676–680.

53 S. M. Yang, S. Lee, J. Jian, W. Zhang, P. Lu, Q. Jia, H. Wang, T. W. Noh, S. V. Kalinin and J. L. MacManus-Driscoll, Strongly Enhanced Oxygen Ion Transport Through Samarium-doped CeO₂ Nanopillars in Nanocomposite Films, *Nat. Commun.*, 2015, **6**, 8588.

54 P. P. Dholabhai, G. Pilania, J. A. Aguiar, A. Misra and B. P. Uberuaga, Termination Chemistry-driven Dislocation Structure at SrTiO₃/MgO Heterointerfaces, *Nat. Commun.*, 2014, **5**, 5043.

55 P. P. Dholabhai, E. Martinez, N. T. Brown and B. P. Uberuaga, On the Mobility of Carriers at Semi-coherent

Oxide Heterointerfaces, *Phys. Chem. Chem. Phys.*, 2017, **19**, 23122.

56 P. P. Dholabhai, J. A. Aguiar, A. Misra and B. P. Uberuaga, Defect Interactions with Stepped CeO_2/$SrTiO_3$ Interfaces: Implications for Radiation Damage Evolution and Fast Ion Conduction, *J. Chem. Phys.*, 2014, **140**, 194701.

57 P. P. Dholabhai and B. P. Uberuaga, Beyond Coherent Oxide Heterostructures: Atomic-scale Structure of Misfit Dislocations, *Adv. Theory Simul.*, 2019, **2**, 1900078.

58 W. Ebmeyer and P. P. Dholabhai, High-throughput prediction of oxygen vacancy defect migration near misfit dislocations in $SrTiO_3$/$BaZrO_3$ heterostructures, *Mater. Adv.*, 2024, **5**, 315–328.

59 C. Marzano and P. P. Dholabhai, High-throughput prediction of thermodynamic stabilities of dopant-defect clusters at misfit dislocations in perovskite oxide heterostructures, *J. Phys. Chem. C*, 2023, **127**, 15988–15999.

60 P. P. Dholabhai, Oxygen Vacancy Formation and Interface Charge Transfer at Misfit Dislocations in Gd-Doped CeO_2/MgO Heterostructures, *J. Phys. Chem. C*, 2022, **126**, 11735–11750.

61 A. Lopez-Bezanilla, P. Ganesh and P. B. Littlewood, Plentiful magnetic moments in oxygen deficient $SrTiO_3$, *APL Mater.*, 2015, **3**, 100701.

62 A. B. Muñoz-García, A. M. Ritzmann, M. Pavone, J. A. Keith and E. A. Carter, Oxygen Transport in Perovskite-Type Solid Oxide Fuel Cell Materials: Insights from Quantum Mechanics, *Acc. Chem. Res.*, 2014, **47**(11), 3340.

63 G. Pilania, P. P. Dholabhai and B. P. Uberuaga, Role of Symmetry, Geometry, and Termination Chemistry on Misfit Dislocation Patterns at Semicoherent Heterointerfaces, *Matter*, 2020, **2**, 1324–1337.

64 W. Ebmeyer, P. Hatton, B. P. Uberuaga and P. P. Dholabhai, Influence of misfit dislocations on ionic conductivity at oxide interfaces, *J. Mater. Chem. A*, 2024, **12**, 21252.

65 P. Hohenberg and W. Kohn, Inhomogeneous Electron Gas, *Phys. Rev.*, 1964, **136**, B864.

66 W. Kohn and L. J. Sham, Self-Consistent Equations Including Exchange and Correlation Effects, *Phys. Rev.*, 1965, **140**, A1133.

67 J. P. Perdew, K. Burke and M. Ernzerhof, Generalized Gradient Approximation Made Simple, *Phys. Rev. Lett.*, 1996, **77**, 3865.

68 P. E. Bhöchl, Projector augmented-wave method, *Phys. Rev. B: Condens. Matter Mater. Phys.*, 1994, **50**, 17953.

69 G. Kresse and J. Hafner, *Ab Initio* Molecular Dynamics for Liquid Metals, *Phys. Rev. B: Condens. Matter Mater. Phys.*, 1993, **47**, 558.

70 G. Kresse and J. Furthmuller, Efficient Iterative Schemes for *Ab Initio* Total-energy Calculations Using a Plane-wave Basis Set, *Phys. Rev. B: Condens. Matter Mater. Phys.*, 1996, **54**, 11169.

71 S. L. Dudarev, G. A. Botton, S. Y. Savrasov, C. J. Humphreys and A. P. Sutton, Electron-energy-loss Spectra and the Structural Stability of Nickel Oxide: An LSDA + U Study, *Phys. Rev. B: Condens. Matter Mater. Phys.*, 1998, **57**, 1505–1509.

72 H. J. Monkhorst and J. D. Pack, Special points for Brillouin-zone integrations, *Phys. Rev. B*, 1976, **13**, 5188.

73 P. P. Dholabhai, Atomic-scale Structure of Misfit Dislocations in $CeO2$/MgO Heterostructure and Thermodynamic Stability of Dopant-defect Complexes at the Heterointerface, *Phys. Chem. Chem. Phys.*, 2019, **21**, 20878.

74 L. Chen, C. L. Chen, X. Chen, W. Donner, S. W. Liu, Y. Lin, D. X. Huang and A. J. Jacobson, Electrical properties of a highly oriented, textured thin film of the ionic conductor δ on (001) MgO, *Appl. Phys. Lett.*, 2003, **83**, 4737.

75 C. A. Copetti, J. Schubert, A. M. Klushin, S. Bauer, W. Zander, Ch Buchal, J. W. Seo, F. Sanchez and M. Bauer, Graphoepitaxy of CeO_2 on MgO and its application to the fabrication of 45° grain boundary Josephson junctions of $YBa_2Cu_3O_{7-x}$, *J. Appl. Phys.*, 1995, **78**, 5058.

76 A. Fluri, D. Pergolesi, V. Roddatis, A. Wokaun and T. Lippert, In situ stress observation in oxide films and how tensile stress influences oxygen ion conduction, *Nat. Commun.*, 2016, **7**, 10692.

77 L. Zhang, I. Bredeson, A. Y. Birenbaum, P. R. C. Kent, V. R. Cooper, P. Ganesh and H. Xu, Oxygen vacancy formation energies in $PbTiO_3$/$SrTiO_3$ superlattice, *Phys. Rev. Mater.*, 2018, **2**, 064409.

78 S. Choudhury, D. Morgan and B. P. Uberuaga, Massive Interfacial Reconstruction at Misfit Dislocations in Metal/Oxide Interfaces, *Sci. Rep.*, 2014, **4**, 6533.

79 M. Li, J. Li, L. Q. Chen, B. L. Gu and W. Duan, Effects of strain and oxygen vacancies on the ferroelectric and anti-ferrodistortive distortions in $PbTiO_3$/$SrTiO_3$ superlattice, *Phys. Rev. B: Condens. Matter Mater. Phys.*, 2015, **92**, 115435.

80 B. Baldassarri, J. He, X. Qian, E. Mastronardo, S. Griesemer, S. M. Haile and C. Wolverton, Accuracy of DFT computed oxygen-vacancy formation energies and high-throughput search of solar thermochemical water-splitting compounds, *Phys. Rev. Mater.*, 2023, **7**, 065403.

81 M. M. Kuklja, E. A. Kotomin, R. Merkle, Y. A. Mastrikov and J. Maier, Combined theoretical and experimental analysis of processes determining cathode performance in solid oxide fuel cells, *Phys. Chem. Chem. Phys.*, 2013, **15**, 5443.

82 K. T. Butler, G. Sai Gautam and P. Canepa, Designing interfaces in energy materials applications with first-principles calculations, *npj Comput. Mater.*, 2019, **5**, 19.

83 Y. Wang, X. Liu, Q. Yang, Y. Liu, Z. Li, B. Guo, H. Mao, R. D. K. Misra and H. Xu, First principles calculation of interfacial stability, energy, and elemental diffusional stability of Fe (111)/Al_2O_3 (0001) interface, *AIP Adv.*, 2019, **9**, 125313.

84 D. A. Andersson, S. I. Simak, N. V. Skorodumova, I. A. Abrikosov and B. Johansson, Optimization of ionic conductivity in doped ceria, *Proc. Natl. Acad. Sci. U. S. A.*, 2006, **103**, 3518.

85 N. Tsunoda, Y. Kumagai and F. Oba, Stabilization of small polarons in $BaTiO_3$ by local distortions, *Phys. Rev. Mater.*, 2019, **3**, 114602.